

## Three Saturn-mass Microlensing Planets Identified through Signals from Peripheral-caustic Perturbations

CHEONCHO HAN<sup>\*</sup>,<sup>1</sup> CHUNG-UK LEE,<sup>2</sup> ANDRZEJ UDALSKI<sup>3</sup> AND IAN A. BOND<sup>4</sup>

(LEADING AUTHORS)

MICHAEL D. ALBROW,<sup>5</sup> SUN-JU CHUNG,<sup>2</sup> ANDREW GOULD,<sup>6</sup> YOUN KIL JUNG,<sup>2,7</sup> KYU-HA HWANG,<sup>2</sup> YOON-HYUN RYU,<sup>2</sup> YOSSI SHVARTZVALD,<sup>8</sup> IN-GU SHIN,<sup>9</sup> JENNIFER C. YEE,<sup>10</sup> WEICHENG ZANG,<sup>9</sup> HONGJING YANG,<sup>9</sup> DOEON KIM,<sup>1</sup> DONG-JIN KIM,<sup>2</sup> SANG-MOK CHA,<sup>2,11</sup> SEUNG-LEE KIM,<sup>2</sup> DONG-JOO LEE,<sup>2</sup> YONGSEOK LEE,<sup>2,11</sup> BYEONG-GON PARK,<sup>2</sup> KYEONGSOO HONG<sup>2</sup> AND RICHARD W. POGGE<sup>6</sup>

(KMTNET COLLABORATION)

PRZEMEK MRÓZ,<sup>3</sup> MICHAŁ K. SZYMAŃSKI,<sup>3</sup> JAN SKOWRON,<sup>3</sup> RADOSŁAW POLESKI,<sup>3</sup> IGOR SOSZYŃSKI,<sup>3</sup> PAWEŁ PIETRUKOWICZ,<sup>3</sup> SZYMON KOZŁOWSKI,<sup>3</sup> KRZYSZTOF A. RYBICKI,<sup>3</sup> PATRYK IWANEK,<sup>3</sup> KRZYSZTOF ULACZYK,<sup>12</sup> MARCIN WRONA,<sup>3,13</sup> MARIUSZ GROMADZKI<sup>3</sup> AND MATEUSZ J. MRÓZ<sup>3</sup>

(OGLE COLLABORATION)

FUMIO ABE,<sup>14</sup> DAVID P. BENNETT,<sup>15,16</sup> APARNA BHATTACHARYA,<sup>15,16</sup> RYUSEI HAMADA,<sup>17</sup> YUKI HIRAO,<sup>18</sup> ASAHI IDEI,<sup>17</sup> STELA ISHITANI SILVA,<sup>15</sup> SHUMA MAKIDA,<sup>17</sup> SHOTA MIYAZAKI,<sup>19</sup> YASUSHI MURAKI,<sup>14</sup> TUTUMI NAGAI,<sup>17</sup> TOGO NAGANO,<sup>17</sup> SEIYA NAKAYAMA,<sup>17</sup> MAYU NISHIO,<sup>17</sup> KANSUKE NUNOTA,<sup>17</sup> RYO OGAWA,<sup>17</sup> RYUNOSUKE OISHI,<sup>17</sup> YUI OKUMOTO,<sup>17</sup> GREG OLMSCHENK,<sup>15</sup> CLÉMENT RANC,<sup>20</sup> NICHOLAS J. RATTENBURY,<sup>21</sup> YUKI SATOH,<sup>22</sup> TAKAHIRO SUMI,<sup>17</sup> DAISUKE SUZUKI,<sup>17</sup> TAKUTO TAMAOKI,<sup>17</sup> SEAN K. TERRY,<sup>15,16</sup> PAUL J. TRISTRAM,<sup>23</sup> AIKATERINI VANDOROU<sup>15,16</sup> AND HIBIKI YAMA<sup>17</sup>

(THE MOA AND PRIME COLLABORATION)

<sup>1</sup>Department of Physics, Chungbuk National University, Cheongju 28644, Republic of Korea

<sup>2</sup>Korea Astronomy and Space Science Institute, Daejon 34055, Republic of Korea

<sup>3</sup>Astronomical Observatory, University of Warsaw, Al. Ujazdowskie 4, 00-478 Warsaw, Poland

<sup>4</sup>School of Mathematical and Computational Sciences, Massey University, Auckland 0745, New Zealand

<sup>5</sup>University of Canterbury, Department of Physics and Astronomy, Private Bag 4800, Christchurch 8020, New Zealand

<sup>6</sup>Department of Astronomy, Ohio State University, 140 West 18th Ave., Columbus, OH 43210, USA

<sup>7</sup>University of Science and Technology, Daejeon 34113, Republic of Korea

<sup>8</sup>Department of Particle Physics and Astrophysics, Weizmann Institute of Science, Rehovot 76100, Israel

<sup>9</sup>Department of Astronomy, Westlake University, Hangzhou 310030, Zhejiang Province, China

<sup>10</sup>Center for Astrophysics | Harvard & Smithsonian 60 Garden St., Cambridge, MA 02138, USA

<sup>11</sup>School of Space Research, Kyung Hee University, Yongin, Gyeonggi 17104, Republic of Korea

<sup>12</sup>Department of Physics, University of Warwick, Gibbet Hill Road, Coventry, CV4 7AL, UK

<sup>13</sup>Villanova University, Department of Astrophysics and Planetary Sciences, 800 Lancaster Ave., Villanova, PA 19085, USA

<sup>14</sup>Institute for Space-Earth Environmental Research, Nagoya University, Nagoya 464-8601, Japan

<sup>15</sup>Code 667, NASA Goddard Space Flight Center, Greenbelt, MD 20771, USA

<sup>16</sup>Department of Astronomy, University of Maryland, College Park, MD 20742, USA

<sup>17</sup>Department of Earth and Space Science, Graduate School of Science, Osaka University, Toyonaka, Osaka 560-0043, Japan

<sup>18</sup>Institute of Astronomy, Graduate School of Science, The University of Tokyo, 2-21-1 Osawa, Mitaka, Tokyo 181-0015, Japan

<sup>19</sup>Institute of Space and Astronautical Science, Japan Aerospace Exploration Agency, 3-1-1 Yoshinodai, Chuo, Sagamihara, Kanagawa 252-5210, Japan

<sup>20</sup>Sorbonne Université, CNRS, UMR 7095, Institut d'Astrophysique de Paris, 98 bis bd Arago, 75014 Paris, France

<sup>21</sup>Department of Physics, University of Auckland, Private Bag 92019, Auckland, New Zealand

<sup>22</sup>College of Science and Engineering, Kanto Gakuin University, Yokohama, Kanagawa 236-8501, Japan

<sup>23</sup>University of Canterbury Mt. John Observatory, P.O. Box 56, Lake Tekapo 8770, New Zealand

## ABSTRACT

Corresponding author: [cheoncho@astroph.chungbuk.ac.kr](mailto:cheoncho@astroph.chungbuk.ac.kr)

Corresponding author: [leecu@kasi.re.kr](mailto:leecu@kasi.re.kr)

We present the discovery and analysis of three microlensing planets identified through brief positive anomalies on the wings of their light curves. The events, KMT-2021-BLG-0852, KMT-2024-BLG-2005, and KMT-2025-BLG-0481, were detected in high-cadence survey data from the KMTNet, OGLE, MOA, and PRIME collaborations. The anomaly morphologies are consistent with major-image perturbations induced by planetary-mass companions located near the peripheral caustic. A systematic exploration of model degeneracies, including binary-source scenarios, higher mass-ratio binary lenses, and the inner–outer caustic degeneracy, firmly establishes the planetary origin of each signal. Measurements of the angular Einstein radius and event timescale, combined with Bayesian priors from a Galactic model, yield the physical parameters of each system. The hosts are low-mass stars ( $0.12$ – $0.75 M_{\odot}$ ), while the companions are Saturn-mass planets ( $0.16$ – $0.59 M_{\mathrm{J}}$ ) projected at separations of  $1.1$ – $7.8$  au, placing them beyond the snowline of their hosts. These results demonstrate the capability of microlensing to detect and characterize cold giant planets around low-mass stars at kpc distances, populating the critical transition region between ice giants and gas giants.

*Keywords:* Gravitational microlensing exoplanet detection (2147)

## 1. INTRODUCTION

The remarkable diversity of the known exoplanet population, encompassing terrestrial worlds, super-Earths, ice giants, and gas giants, provides a vital laboratory for testing theories of planetary formation and evolution (Winn & Fabrycky 2015). While super-Jupiters (with masses  $M \gtrsim 5 M_{\mathrm{J}}$ ) mark the upper boundary of the planetary mass scale, a comprehensive mapping of planetary demographics requires a focus on the transition between ice giants and massive gas giants. In this context, identifying Saturn-mass planets in the cold outer regions of their host systems is essential for constraining the efficiency of core formation and subsequent gas accretion beyond the snowline, where the condensation of volatiles increases the surface density of solids (Kennedy & Kenyon 2008).

Within the framework of core accretion theory, Saturn-mass planets represent a distinctive transition regime. Standard models predict that once a solid core reaches a critical mass of  $\sim 10$ – $15 M_{\oplus}$ , it triggers a phase of runaway gas accretion (Stevenson 1982; Pollack et al. 1996). While Jupiter-mass planets are the canonical result of sustained growth, Saturn-mass planets likely represent cases for which this rapid accumulation was interrupted either by the dissipation of the protoplanetary disk or by disk-driven migration that moved the protoplanet into a gas-depleted region (Ida & Lin 2004; Alibert et al. 2005). Consequently, Saturn-mass planets are not merely small Jupiters. They are expected to retain significantly higher core-to-envelope mass fractions compared to their more massive counterparts (Fortney et al. 2007). This makes them sensitive probes of the precise timing of disk depletion and of the underlying physics of solid core assembly.

While the radial-velocity and transit techniques have been extraordinarily successful in characterizing exoplanets on short to moderate orbital periods, they become progressively less sensitive to planets in the cold, outer regions of planetary systems. Gravitational microlensing, by contrast, provides a uniquely powerful and complementary probe of cold planets at wide separations, with peak sensitivity to companions located near and beyond the snowline (Mao & Paczyński 1991; Gould & Loeb 1992; Gaudi 2012). Moreover, because the microlensing signal depends on the gravitational field of the lens rather than its emitted light, the method is largely insensitive to host luminosity. This enables the detection of planets orbiting low-mass stars and even substellar hosts such as brown dwarfs, thereby offering a relatively unbiased view of planetary demographics across a broad range of host masses.

In this paper, we report the discovery of three Saturn-mass planets orbiting low-mass stars, identified through the analysis of short-term anomalies in microlensing light curves obtained from high-cadence survey observations. In each case, the planetary signature appears as a positive deviation from the corresponding single-lens model, confined to the wing regions of the light curve and lasting for only a brief interval. We present a detailed analysis of these events, exploring the underlying lensing geometries that give rise to such features. We explore a range of model degeneracies that can complicate the interpretation of planetary signals producing anomalies with similar morphologies.

## 2. DATA

Short-term anomalies in the events analyzed in this work were first identified during our inspection of microlensing events detected by the Korea Microlens-

**Table 1.** Coordinates and event ID correspondence.

KMTNet ID	(RA, DEC) <sub>J2000</sub>	( $l, b$ )	Other ID
KMT-2021-BLG-0852	(17:43:19.48, $-33:53:30.62$ )	( $-4^{\circ}4815, -2^{\circ}1734$ )	...
KMT-2024-BLG-2005	(17:53:37.94, $-28:54:03.53$ )	( $+0^{\circ}9312, -1^{\circ}4860$ )	PRIME-2024-BLG-088
KMT-2025-BLG-0481	(17:41:25.44, $-34:22:18.30$ )	( $-5^{\circ}0970, -2^{\circ}0913$ )	OGLE-2025-BLG-0543

ing Telescope Network (KMTNet) survey (Kim et al. 2016), namely KMT-2021-BLG-0852, KMT-2024-BLG-2005, and KMT-2025-BLG-0481. We subsequently examined whether these events were also monitored by other microlensing surveys. We found that KMT-2025-BLG-0481 was independently discovered by the Optical Gravitational Lensing Experiment (OGLE) (Udalski et al. 2015), with the designation OGLE-2025-BLG-0543. The event KMT-2024-BLG-2005 was also observed by the PRime-focus Infrared Microlensing Experiment (PRIME) survey (Sumi et al. 2025) and labeled PRIME-2024-BLG-088. Although this event was not independently reported by the OGLE and Microlensing Observations in Astrophysics (MOA) surveys (Bond et al. 2001; Sumi et al. 2003), we recovered their data through subsequent photometric re-reductions of the field.

In Table 1, we list the equatorial and Galactic coordinates of the events, together with the corresponding event identifiers adopted by the different surveys. In all cases, the events were first identified by KMTNet, and we therefore refer to them throughout this work using the KMTNet designations.

Observations of the events by the four microlensing surveys were carried out using the following facilities and instrumentation. KMTNet consists of three 1.6-m wide-field optical telescopes strategically distributed across the Southern Hemisphere in Chile (KMTC), South Africa (KMTS), and Australia (KMTA). Each KMTNet telescope is equipped with an  $18\text{k} \times 18\text{k}$  mosaic CCD camera that provides a  $4 \text{ deg}^2$  field of view. OGLE operates the 1.3-m Warsaw Telescope at Las Campanas Observatory in Chile with a 32-CCD mosaic camera covering  $1.4 \text{ deg}^2$ . MOA conducts observations with the 1.8-m MOA-II telescope at Mt. John Observatory in New Zealand using the MOA-cam3 prime-focus camera, which comprises ten  $2\text{k} \times 4\text{k}$  CCDs and covers  $2.2 \text{ deg}^2$ . Finally, PRIME utilizes a 1.8-m prime-focus near-infrared telescope in South Africa equipped with PRIME-Cam, a four-detector H4RG-10 ( $4096 \times 4096$ ) NIR mosaic delivering  $1.45 \text{ deg}^2$ . Observations by KMTNet and OGLE were conducted primarily in the Cousins  $I$  band, whereas MOA observations were obtained in the

custom MOA- $R$  band. For these surveys, a subset of the images was also taken in the  $V$  band to determine the source color. PRIME observations were carried out in the  $H$  band.

The image reduction and photometry were carried out using the standard pipelines of the individual surveys. To obtain precise photometry in the crowded Galactic bulge fields, these pipelines commonly employ difference image analysis, in which each science image is registered to a high-quality reference frame, PSF-matched through kernel convolution, and subtracted to yield high-precision differential flux measurements for variable sources (Tomaney & Croots 1996; Alard & Lupton 1998; Woźniak 2000). For light-curve modeling, the originally reported photometric uncertainties for each data set were renormalized to account for underestimated systematics and to ensure statistically consistent weighting, following the prescription of Yee et al. (2012).

### 3. ANALYSIS

In gravitational microlensing events, planetary signals can be classified as central or peripheral perturbations, depending on which caustic produces the deviation in the lensing light curve. A planetary lens system generates two distinct types of caustics: central caustics and planetary (peripheral) caustics. Central caustics form in the immediate vicinity of the host star, and the perturbations they induce therefore tend to occur near the peak of high-magnification events, producing central perturbations (Griest & Safizadeh 1998). By contrast, planetary caustics occur at larger separations from the host star, and the associated deviations often appear in the wing regions of the microlensing light curve. Such deviations are referred to here as peripheral perturbations.

Planetary signals arising from peripheral perturbations can be further subdivided into major-image and minor-image perturbations. In a single-lens event, the source is split into two images: a major image that forms outside the Einstein ring on the same side as the planet and a minor image that forms inside the Einstein ring on the opposite side. As the lens–source relative motion proceeds, these images move along predictable trajectories. A planetary deviation occurs when the planet lies

**Table 2.** Lensing parameters.

Parameter	KMT-2021-BLG-0852			KMT-2024-BLG-2005		KMT-2025-BLG-0481
	Inner	Outer	1L2S	Solution 1	Solution 2	
$\chi^2/N_{\text{data}}$	1841.8/1846	2046.8/1846	2396.8/1846	9874.7/9942	10204.9/9942	680.0/679
$t_0$ (HJD')	9350.551 $\pm$ 0.018	9351.327 $\pm$ 0.016	9418.164 $\pm$ 0.693	524.992 $\pm$ 0.015	524.518 $\pm$ 0.019	783.540 $\pm$ 0.046
$u_0$	0.01757 $\pm$ 0.00050	-0.02796 $\pm$ 0.00226	-1.99 $\pm$ 0.13	0.1038 $\pm$ 0.0029	0.0948 $\pm$ 0.0019	0.2107 $\pm$ 0.0067
$t_E$ (days)	59.71 $\pm$ 1.74	45.09 $\pm$ 2.94	38.47 $\pm$ 2.81	28.82 $\pm$ 0.62	30.57 $\pm$ 0.51	16.02 $\pm$ 0.33
$s$	2.225 $\pm$ 0.031	2.785 $\pm$ 0.121	...	1.1408 $\pm$ 0.0030	1.1013 $\pm$ 0.0017	1.3689 $\pm$ 0.0096
$q$ ( $10^{-3}$ )	0.622 $\pm$ 0.031	0.418 $\pm$ 0.038	...	1.29 $\pm$ 0.10	11.49 $\pm$ 0.45	2.58 $\pm$ 0.16
$\alpha$ (rad)	4.068 $\pm$ 0.010	4.096 $\pm$ 0.021	...	5.7941 $\pm$ 0.0038	-0.0612 $\pm$ 0.0052	3.4417 $\pm$ 0.0059
$\rho$ ( $10^{-3}$ )	6.80 $\pm$ 0.73	27.17 $\pm$ 2.19	...	5.50 $\pm$ 0.51	6.29 $\pm$ 0.36	4.56 $\pm$ 0.30
$t_{0,2}$	...	...	9351.2371 $\pm$ 0.0062	...	...	...
$u_{0,2}$ ( $10^{-3}$ )	...	...	-0.68 $\pm$ 01.36	...	...	...
$\rho_2$ ( $10^{-3}$ )	...	...	13.92 $\pm$ 0.93	...	...	...
$q_F$	...	...	0.0030 $\pm$ 0.0006	...	...	...

NOTE— For KMT-2021-BLG-0852,  $\text{HJD}' \equiv \text{HJD} - 2450000$ ; for the other events,  $\text{HJD}' \equiv \text{HJD} - 2460000$ .

close to the trajectory of one of these images, producing an distortion in the magnification pattern.

A major-image perturbation occurs when a wide-separation planet (with a projected separation larger than the Einstein radius) lies close to the major image produced by the host lens. Conversely, a minor-image perturbation arises when a close-separation planet (with a projected separation smaller than the Einstein radius) perturbs the minor image. These two classes of perturbations produce distinct observational signatures: perturbations of the major image typically increase the magnification, leading to positive deviations from the single-lens light curve, whereas, in most cases, perturbations of the minor image decrease the magnification, producing negative deviations. For examples of planetary microlensing events exhibiting major- and minor-image perturbations, see Han et al. (2024a) and Han et al. (2024b).

In all three events analyzed here, the signals manifest as short-duration positive anomalies in the wings of the light curves. If these deviations are planetary in origin, their morphology provides a useful diagnostic of the underlying mechanism. First, their occurrence in the wings strongly suggests that they arise from peripheral caustics rather than central caustics. Second, the fact that the deviations are positive most likely indicates that the major image is perturbed. Taken together, these characteristics most naturally point to wide-separation planets that perturb the major image as it passes near the associated peripheral caustic. Motivated by this interpretation, we model each event using a binary-lens single-source (2L1S) framework in which the lens consists of a host star and a companion in the planetary-mass regime.

We perform the modeling by searching for the set of lensing parameters that best reproduces the observed

light curve. For a lensing event produced by a binary lens (a host star and a planet), the light curve is described by seven basic parameters. The three parameters ( $t_0, u_0, t_E$ ) characterize the source-lens encounter, where  $t_0$  is the time of closest approach,  $u_0$  is the impact parameter (normalized to the angular Einstein radius  $\theta_E$ ), and  $t_E$  is the event timescale, defined as the time required for the source to traverse an angular distance of  $\theta_E$ . The binary-lens geometry is specified by  $(s, q)$ , where  $s$  is the projected separation between the lens components (in units of  $\theta_E$ ) and  $q$  is their mass ratio. The parameter  $\alpha$  denotes the angle between the binary-lens axis and the source trajectory. In many planetary events, the anomaly is affected by finite-source effects because the signal arises when the source approaches or crosses a caustic induced by the planet. To account for these effects, we include an additional parameter  $\rho$ , which is defined as the ratio of the angular source radius ( $\theta_*$ ) to  $\theta_E$ .

In our analyses, we explore alternative origins of short-term anomalies and address the associated degeneracies, which are essential for correctly interpreting these features. A particularly important non-planetary channel is the single-lens binary-source (1L2S) scenario, in which the observed flux is the superposition of two unresolved sources (Griest & Hu 1992). The primary source produces the main microlensing event, while a fainter companion can briefly contribute additional magnified light if it passes closer to the lens and/or reaches peak magnification at a different time. This typically generates a short, positive bump that can closely mimic a planetary major-image perturbation when the flux ratio is small, making 1L2S a well-known false-positive channel in microlensing planet searches (Gaudi 1998; Shin et al. 2019). In addition to the three parameters of a single-

lens (1L1S) event,  $t_0$ ,  $u_0$ , and  $t_E$ , modeling a 1L2S event requires four additional parameters:  $t_{0,2}$ ,  $u_{0,2}$ ,  $\rho_2$ , and  $q_F$ . The first two specify the time of closest approach and the corresponding impact parameter of the second source star ( $S_2$ ). The third parameter,  $\rho_2$ , represents the normalized angular radius of  $S_2$ , and the final parameter,  $q_F$ , denotes the flux ratio between the two source stars (Hwang et al. 2013).

Another non-planetary possibility is that the anomaly is produced not by a planet but by a higher mass-ratio binary lens, such as a low-mass stellar companion or a brown dwarf. Although such systems can generate large caustics, they may still produce short-lived anomalies if the source probes only a localized region of the magnification pattern, for example during a cusp approach or a grazing encounter with a caustic tip. In these cases, the perturbation timescale is set by the small spatial extent of the region sampled by the source trajectory, allowing a brief deviation even when the overall caustic structure is large.

Finally, even when a planetary interpretation is favored, the inferred parameters may not be unique because of degeneracies among different planetary configurations. In particular, the inner–outer degeneracy arises because a planetary anomaly can often be reproduced nearly equally well by source trajectories passing on either the inner (host-facing) or outer (host-opposing) side of the peripheral caustic (Gaudi & Gould 1997). Moreover, when anomalies are incompletely covered, additional accidental degeneracies may arise, as illustrated by Hwang et al. (2018). We therefore perform a thorough exploration of all plausible degenerate solutions. In the following three sections, we present the modeling details for each event and the results obtained from these analyses.

#### 4. KMT-2021-BLG-0852

Figure 1 shows the light curve of the microlensing event KMT-2021-BLG-0852. The light curve consists of two distinct components: (1) a broad main feature peaking at  $\text{HJD}' \equiv \text{HJD} - 2450000 \simeq 9418$  with a low maximum magnification of  $A_{\text{max}} \sim 1.15$ , and (2) a short-term anomaly centered near  $\text{HJD}' \simeq 9351$  with a relatively high peak. The anomaly comprises two sub-features: a weak bump at  $\text{HJD}' \simeq 9349.7$  followed by a stronger peak at  $\text{HJD}' \simeq 9351.2$ .

The event was first identified by the KMTNet survey on 2021 May 17 ( $\text{HJD}' \simeq 9351$ ), coincident with the peak of the anomaly, and was subsequently monitored exclusively by KMTNet. The source lies in the KMTNet field BLG17, which was observed at a cadence of 1.0 hr.

The extinction toward the field is  $A_I \sim 3.0$ , and the baseline  $I$ -band magnitude is  $I_{\text{base}} = 18.75$ .

The light curve features are characteristic of planetary microlensing, exhibiting a localized anomaly produced by a planet orbiting the primary lens, set against a broader magnification profile produced by the host. We therefore adopted a 2L1S modeling approach, which successfully reproduces all features of the observed event, including the short-duration anomaly.

The best-fit model is shown as the solid curve in Figure 1, and the corresponding parameters are listed in Table 2, together with the  $\chi^2$  value and the number of data points,  $N_{\text{data}}$ . We define  $t_0$  as the epoch of the the closest approach to the center of the peripheral caustic and  $u_0$  is the impact parameter to this approach. The best-fit binary-lens parameters are  $(s, q) \sim (2.2, 0.6 \times 10^{-3})$ , indicating that the anomaly was induced by a planetary-mass companion at a projected separation of  $\sim 2.2$  times the Einstein radius. The event timescale is approximately 60 days. Although the source trajectory only grazes the caustic, the normalized source radius was nevertheless well measured to be  $\rho \sim (6.8 \pm 0.7) \times 10^{-3}$ .

The corresponding lens-system geometry is illustrated in the insets of the lower panel of Figure 1. The right inset shows the positions of the lens components and caustic structure, while the left inset provides a close-up view of the caustic region. The planet produces a small four-cusp caustic displaced from the host by  $s - 1/s \sim 1.78$ . The source trajectory crosses the planet–host axis at an incidence angle of  $\sim 53^\circ$ , and the anomaly occurs as the source approaches the planet-induced caustic. The acute trajectory causes the source to first approach the upper cusp, creating a minor bump, before passing the inner side of the strong on-axis cusp to produce the primary peak of the anomaly. These successive cusp approaches naturally explain the observed two-component structure of the anomaly.

We investigated possible degeneracies in the solution. First, we examined the ambiguity with an alternative model in which the source passes the outer region of the caustic. In the upper panel of Figure 1, the model curve for the outer solution is represented by a dotted line overlaid on the data and its associated lensing parameters are summarized in Table 2. The outer solution provides a significantly poorer fit, with  $\Delta\chi^2 = 205.0$  relative to the preferred inner solution, indicating that the inner–outer degeneracy is clearly resolved. This resolution is due to the caustic geometry: for a source passing the outer side, the strong on-axis cusp is encountered before the weak off-axis cusp. This sequence would produce a light-curve anomaly in which the stronger bump precedes the weaker one, which is the opposite of what is

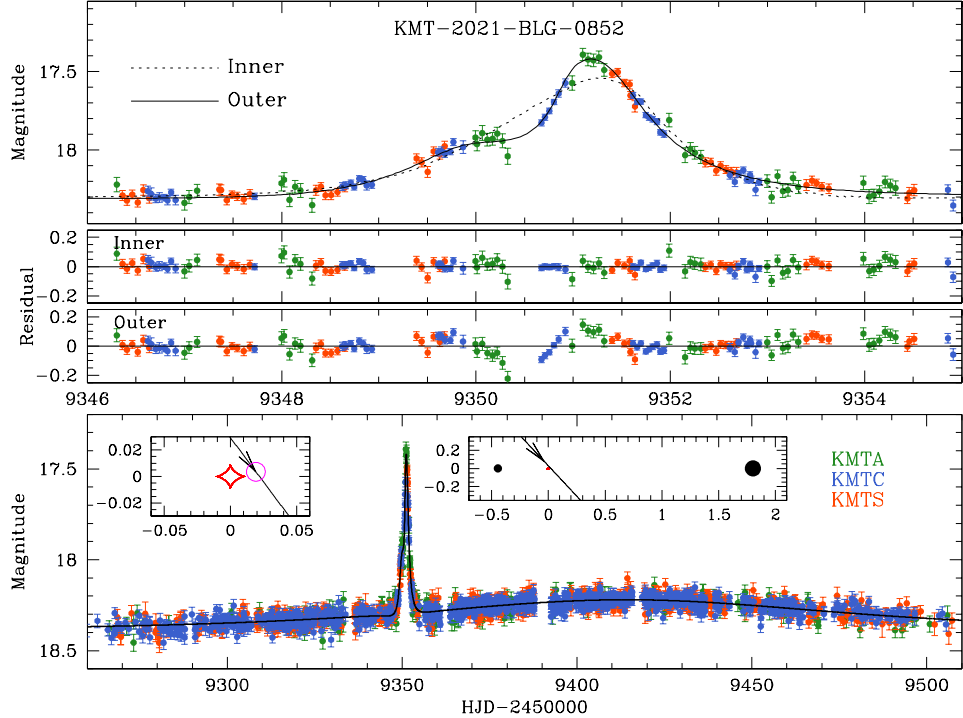


**Figure 1.** Light curve of the microlensing event KMT-2021-BLG-0852. The bottom panel displays the full time-series of the event, while the top panel provides a magnified view of the anomalous region, including the best-fit model curves and residuals for both the inner and outer solutions. The preferred model (inner solution) is overlaid on the data points as a solid curve, and the outer solution is shown as a dotted curve for comparison. The two insets in the bottom panel illustrate the lens-system geometry. The right inset shows the wide-scale configuration, marking the positions of the binary lens components with black filled circles, the caustic structures in red, and the source trajectory with an arrowed line. The left inset shows a close-up of the caustic crossing, where the open magenta circle on the source trajectory indicates the source size scaled to the caustic size.

observed. Therefore, the observed anomaly (weak bump followed by strong bump) is inconsistent with an outer crossing and uniquely supports the inner geometry.

Second, we also tested a binary-source interpretation of the anomaly. The best-fit lensing parameters of the 1L2S model are presented in Table 2. The best-fit 1L2S solution yields  $\chi^2 = 2396.8$ , which is substantially worse than the best-fit planetary model by  $\Delta\chi^2 = 555.0$ . Thus, the anomaly is confidently characterized without any degeneracy in its interpretation.

## 5. KMT-2024-BLG-2005

The light curve of the lensing event KMT-2024-BLG-2005 is shown in Figure 2. Similar to the previous event, it exhibits the same overall morphology, with a short-term anomaly on the rising wing superposed on a broad magnification profile. The anomaly, which lasted for about two days, exhibits two spike features at  $HJD' \equiv HJD - 2460000 \simeq 517.7$  and  $\simeq 519.7$  resulting from caustic crossings by the source. The underlying light curve peaked at  $HJD' \simeq 525$  with a peak magnification  $A_{\max} \sim 9.5$ .

The event was initially identified during its rising phase by the KMTNet survey on 2024 July 29 ( $HJD' = 490$ ). The source is located within the overlapping region of fields BLG02 and BLG42, providing a high combined observational cadence of 15 minutes. The event was subsequently detected by the PRIME survey on 2024 August 02 ( $HJD' \simeq 524$ ) as the light curve approached its peak magnification. Although the event was not alerted in real-time by the MOA and OGLE surveys, we incorporate their data, derived from post-season photometry, into the analysis to ensure more comprehensive coverage of the event.

Guided by the characteristic features of the light curve, we carried out a 2L1S modeling of the light curve. This modeling indicates that the observed anomaly is best explained by a binary lens composed of a host star and a planetary companion. The best-fit binary-lens parameters are  $(s, q) \sim (1.1, 1.3 \times 10^{-3})$ , implying that the planet lies at a projected separation slightly larger than the Einstein radius. The estimated event timescale is  $t_E \sim 29$  days, and the normalized source radius  $\rho \sim 6 \times 10^{-3}$ . The full set of lensing parameters

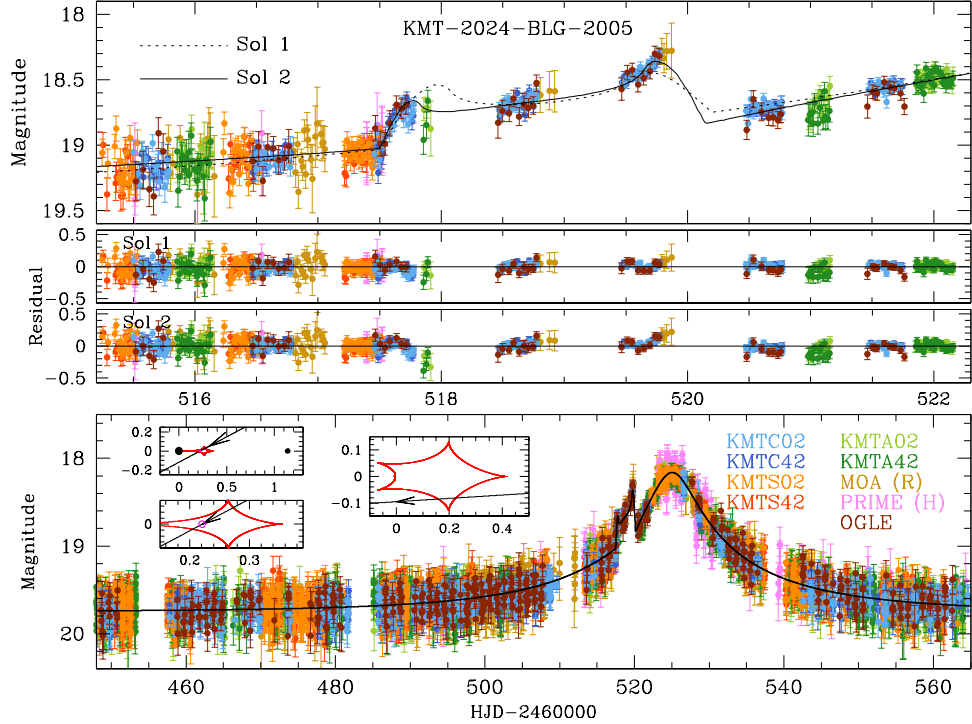


**Figure 2.** Light curve of KMT-2024-BLG-2005. The best-fit model (solution 1) is shown by the solid curve, and the alternative model (solution 2) by the dotted curve. Insets in the lower panel show the lens-system geometries: the two left insets correspond to the wide and enlarged views for solution 1, and the right inset to solution 2.

is summarized in Table 2, and the corresponding best-fit model light curve is presented in Figure 2.

The lens-system configuration of the event is presented in the two left insets of the lower panel of Figure 2. The planets induces a resonant caustic, in which the central and peripheral caustics are connected by a slim bridge. The perturbation occurred as the source crossed the peripheral caustic. The profile of the anomaly between the two caustic spikes deviates from a typical U-shape pattern because the source asymptotically approached the caustic fold after entering the caustic.

We find that the anomaly is uniquely explained by the presented model (Solution 1). A binary-source (1L2S) interpretation is definitively ruled out by the presence of distinct caustic-crossing features in the anomaly. We also explored an alternative binary-lens solution with a higher mass ratio,  $(s, q) \sim (1.10, 0.012)$  (Solution 2). The corresponding lensing parameters are listed in Table 2, and the model light curve, residuals, and lens-system geometry are shown in Figure 2 and its inset. However, Solution 2 provides a substantially worse fit than Solution 1, with  $\Delta\chi^2 = 330.2$ , and we therefore reject this interpretation.

## 6. KMT-2025-BLG-0481

The lensing light curve of KMT-2025-BLG-0481 is shown in Figure 3. The overall profile resembles those of

the two previous events, consisting of a smooth, broad single-lens light curve with a short-duration anomaly superposed upon it. The anomaly lasted for about two days and reached a peak brightness of  $\Delta I \sim 1.5$  mag above the baseline. It is characterized by two prominent features centered at  $\text{HJD}' \simeq 793.5$  and  $\text{HJD}' \simeq 794.4$ , respectively. The underlying light curve peaked at  $\text{HJD}' \simeq 783.5$  with a peak magnification  $A_{\text{max}} \sim 4.8$ .

The event was first detected by the KMTNet survey on 2025 April 14 ( $\text{HJD}' = 779$ ), prior to the main peak, and was subsequently identified by the OGLE survey on April 28 ( $\text{HJD}' = 793$ ), after the peak. The source lies in the KMTNet BLG37 field, which is observed with a 2.5 hr cadence.

Based on a 2L1S modeling of the light curve, we find that the anomaly is of planetary origin. Owing to the detailed structure of the signal, we find that the anomaly is uniquely characterized by binary parameters  $(s, q) \sim (1.4, 2.6 \times 10^{-3})$ , an Einstein timescale of  $t_E \sim 16$  days, and a normalized source radius of  $\rho \sim 4.6 \times 10^{-3}$ . The complete set of lensing parameters is presented in Table 2, and the best-fit model is overlaid on the data in Figure 3.

The geometry of the lens system is illustrated in the insets of Figure 3. The planet produces a small peripheral caustic on the planet side of the host, located at a

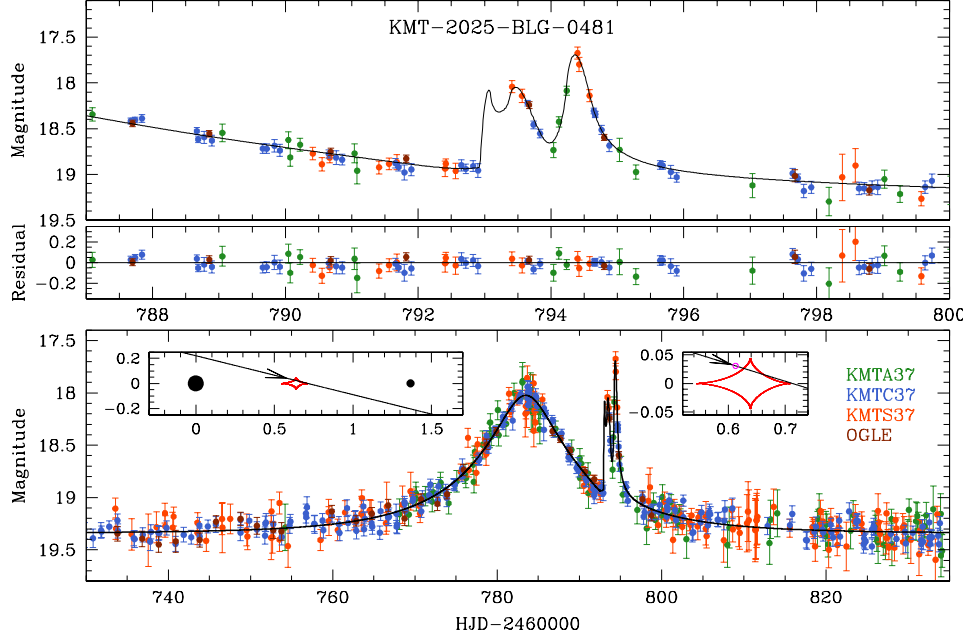


**Figure 3.** Light curve of the event KMT-2025-BLG-0481. Notations are similar to those in Fig. 1.

projected separation of  $s - 1/s \sim 0.64$  from the host. The observed anomaly occurred as the source traversed this caustic. The source first crossed the tip of the caustic, producing the discrete anomaly feature centered at  $\text{HJD}' \sim 793.5$ . It then approached the on-axis cusp on the right side, generating the subsequent feature centered at  $\text{HJD}' \sim 794.4$ . Although a caustic-tip crossing is expected to produce a pair of sharp caustic spikes, the first spike was not recorded owing to gaps in the observational coverage.

## 7. SOURCE STARS AND EINSTEIN RADII

For all three analyzed lensing events, the normalized source radius,  $\rho$ , was measured, enabling an estimation of the angular Einstein radius via the relation

$$\theta_E = \frac{\theta_*}{\rho}. \quad (1)$$

Here,  $\theta_*$  represents the angular radius of the source star, which can be inferred from its de-reddened color and brightness. Determining  $\theta_E$  is essential for characterizing the physical lens parameters, as it is related to the lens mass ( $M$ ) and the lens-source relative parallax ( $\pi_{\text{rel}}$ ) by

$$\theta_E = \sqrt{\kappa M \pi_{\text{rel}}}; \quad \pi_{\text{rel}} = \text{au} \left( \frac{1}{D_L} - \frac{1}{D_S} \right), \quad (2)$$

where  $\kappa = 4G/(c^2 \text{au}) \simeq 8.14 \text{ mas}/M_\odot$ , and  $D_L$  and  $D_S$  denote the distances to the lens and source, respectively. In this section, we therefore determine the de-reddened

source color and magnitude, both to characterize the source stars and to derive the corresponding angular Einstein radii.

The de-reddened color and magnitude of the source were determined following the standard procedure established by Yoo et al. (2004). First, we measured the instrumental color and magnitude of the source,  $(V - I, I)$ , by regressing the  $I$ - and  $V$ -band light curves against the best-fit model. We then placed the source on the instrumental color-magnitude diagram (CMD) constructed from stars in the vicinity of the event. Next, we derived the extinction- and reddening-corrected values,  $(V - I, I)_0$ , using the red giant clump (RGC) centroid in the CMD as a reference. Adopting the intrinsic RGC color and magnitude,  $(V - I, I)_{\text{RGC},0}$ , from Bensby et al. (2013) and Table 1 of Nataf et al. (2013), we measured the offsets in color and magnitude between the source and the RGC centroid,  $\Delta(V - I, I)$ . The dereddened source color and magnitude were then obtained as

$$(V - I, I)_0 = (V - I, I)_{\text{RGC},0} + \Delta(V - I, I). \quad (3)$$

Finally, using the inferred intrinsic color and magnitude, we estimated the angular source radius from the color-surface-brightness relation of Kervella et al. (2004).

For KMT-2025-BLG-0481, the source color could not be measured using the procedure described above because the  $V$ -band light curve was sparsely sampled. In this case, we combined the CMDs constructed from KMTC and Hubble Space Telescope (HST) observations (Holtzman et al. 1998), and then adopted the mean  $(V - I)$  color of stars in the HST CMD lying within

**Table 3.** Source parameters, angular Einstein radius, and relative proper motion.

Parameter	KMT-2021-BLG-0852	KMT-2024-BLG-2005	KMT-2025-BLG-0481
$(V - I)$	$3.275 \pm 0.128$	$2.753 \pm 0.074$	$2.321 \pm 0.177$
$I$	$18.217 \pm 0.014$	$20.820 \pm 0.007$	$20.396 \pm 0.016$
$(V - I, I)_{\text{RGC}}$	$(3.504, 17.576)$	$(2.953, 16.530)$	$(2.593, 16.922)$
$(V - I, I)_{\text{RGC},0}$	$(1.060, 14.610)$	$(1.060, 14.616)$	$(1.060, 14.616)$
$(V - I)_0$	$0.831 \pm 0.134$	$0.860 \pm 0.084$	$0.788 \pm 0.177$
$I_0$	$15.251 \pm 0.025$	$18.689 \pm 0.021$	$18.090 \pm 0.016$
Spectral type	K0III	K0.5V	G8IV
$\theta_*$ (mas)	$3.180 \pm 0.481$	$0.680 \pm 0.074$	$0.828 \pm 0.158$
$\theta_E$ (mas)	$0.467 \pm 0.070$	$0.124 \pm 0.019$	$0.182 \pm 0.037$
$\mu$ (mas/yr)	$2.858 \pm 0.432$	$1.57 \pm 0.24$	$4.14 \pm 0.84$

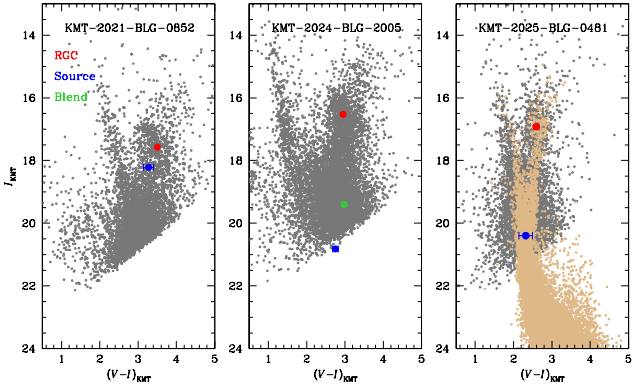


**Figure 4.** Source positions within the instrumental color-magnitude diagrams (CMDs). The red dot represents the centroid of the red giant clump (RGC) used for the photometric calibration of the source color and magnitude. For KMT-2024-BLG-2005, the position of the blended light is also indicated. For KMT-2025-BLG-0481, the CMD is derived from the combination of KMTC (grey) and HST (brown) photometry.

the same range of  $I$ -band magnitude offsets from the RGC centroid.

Figure 4 shows the positions of the source stars in the instrumental CMD, together with the RGC centroid used for photometric calibration. The estimated values of  $(V - I, I)$ ,  $(V - I, I)_{\text{RGC}}$ ,  $(V - I, I)_0$ , and  $(V - I, I)_{\text{RGC},0}$ , along with the inferred spectral types of the source stars, are listed in Table 3. We find that the source star of KMT-2021-BLG-0852 is a K-type giant, whereas the sources of KMT-2024-BLG-2005 and KMT-2025-BLG-0481 are an early K-type main-sequence star and a late G-type subgiant, respectively. Table 3 also lists the estimated angular source radius and Einstein radius, together with the relative lens-source proper motion,  $\mu = \theta_E/t_E$ .

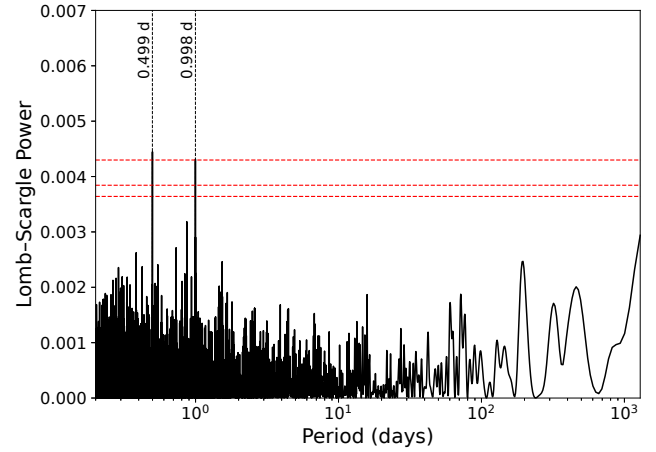


**Figure 5.** Lomb-Scargle periodogram for the baseline flux of KMT-2021-BLG-0852.

Because many giant stars are variable, we check whether the residuals of the KMT-2021-BLG-0852 light curve contain any repeating pattern. To do this, we apply a standard technique for detecting periodic signals in unevenly sampled data. The resulting Lomb-Scargle periodogram is shown in Figure 5. The strongest features occur near 1.0 day and 0.5 day, which are expected artifacts caused by the roughly once-per-day cadence of ground-based observations. Adopting false-alarm probability thresholds of 1%, 5%, and 10%, we find no other periodic signals that exceed the levels expected from random fluctuations.

## 8. PHYSICAL LENS PARAMETERS

A unique determination of the lens mass and distance requires measurements of three lensing observables: the event timescale  $t_E$ , the angular Einstein radius  $\theta_E$ , and the microlens parallax  $\pi_E$ , where  $\pi_E \equiv \pi_{\text{rel}}/\theta_E$ . Together,  $\theta_E$  and  $\pi_E$  yield the lens mass via  $M = \theta_E/(\kappa\pi_E)$

and the lens distance via  $D_L = au/(\pi_E \theta_E + \pi_S)$ , where  $\pi_S$  is the parallax of the source. For the events analyzed here,  $\pi_E$  could not be reliably measured. We therefore infer the physical lens parameters through a Bayesian analysis constrained by the measured lensing observables  $t_E$  and  $\theta_E$ .

The Bayesian analysis begins by adopting a Galactic model that provides priors on the lens population. The model specifies the lens mass function, the spatial density profiles of disk and bulge stars, and the kinematic distributions for each component. These priors define the relative probability of a lens of a given mass residing at a given distance and having a particular transverse velocity along the line of sight. In our analysis, we adopt the lens mass function of [Jung et al. \(2022\)](#) and the Galactic model described by [Jung et al. \(2021\)](#).

Given these priors, we generate a large synthetic ensemble of microlensing events using a Monte Carlo simulation. For each trial, the lens parameters ( $M, D_L$ ) are drawn from the adopted priors, and the source distance  $D_S$  is selected from the source density distribution. A relative transverse velocity is then assigned according to the kinematic model, from which the corresponding microlensing observables ( $t_E, \theta_E$ ) are computed. Each simulated event is weighted by the microlensing event rate (which scales with the lens density and the effective cross section,  $\propto \mu_{\text{rel}} \theta_E$ ) and by the likelihood that its predicted observables match the measured values of  $t_E$  and  $\theta_E$ . Specifically, we assign a likelihood weight of the form

$$L \propto \exp\left(-\frac{\chi^2}{2}\right), \quad (4)$$

where

$$\chi^2 = \frac{(t_E - t_{E,\text{obs}})^2}{\sigma_{t_E}^2} + \frac{(\theta_E - \theta_{E,\text{obs}})^2}{\sigma_{\theta_E}^2}. \quad (5)$$

Here,  $(t_{E,\text{obs}}, \theta_{E,\text{obs}})$  are the observed values of the lensing observables and  $(\sigma_{t_E}, \sigma_{\theta_E})$  are their uncertainties. The posterior probability distributions for  $M$  and  $D_L$  are then constructed from the weighted ensemble. Because these distributions can be asymmetric, we adopt the median as the representative value and the central 68% credible interval as the  $1\sigma$  uncertainty.

For KMT-2021-BLG-0852, the source is relatively bright and is listed in the Gaia DR3 catalog ([Collaboration et al. 2023](#)). It has a Renormalized Unit Weight Error of  $\text{RUWE} = 1.105$ , indicating a good single-star astrometric fit. Gaia measures a proper motion of  $\mu_S = (\mu_{\text{RA}}, \mu_{\text{DEC}}) = (-5.263 \pm 0.572, -5.675 \pm 0.299) \text{ mas yr}^{-1}$ . In our Bayesian analysis, we incorporate this constraint on the source motion when computing the lens-source relative proper motion,  $\mu = \mu_L - \mu_S$ ,

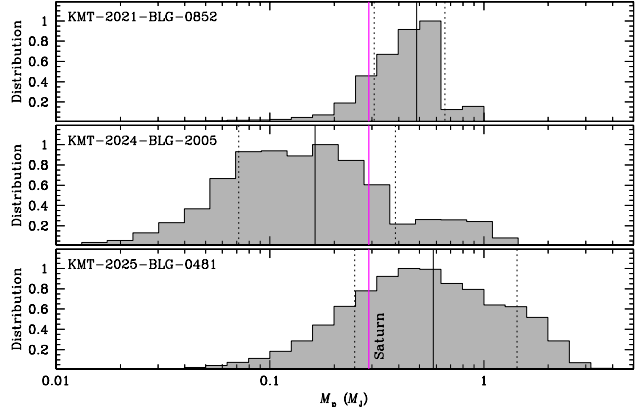


**Figure 6.** Bayesian posterior distributions for the planet mass. In each panel, the solid black vertical line marks the median, and the two dotted lines indicate the  $1\sigma$  credible interval of the distribution. The solid magenta line denotes the mass of Saturn.

where  $\mu_L$  is the proper motion of the lens. This reduces the allowed range of  $\mu$  and hence provides a tighter estimate of  $\theta_E = \mu_{\text{rel}} t_E$ , ultimately yielding a more precise posterior distribution for the lens mass and distance. For the source stars of the other two events, the RUWE values are too high to permit a reliable determination of the source proper motion.

Table 4 lists the inferred physical lens parameters, including the host and planet masses ( $M_h$  and  $M_p$ ), the lens distance ( $D_L$ ), and the projected planet–host separation ( $a_{\perp}$ ). We also provide the relative probabilities that the lens lies in the disk ( $p_{\text{disk}}$ ) or the bulge ( $p_{\text{bulge}}$ ). The inferred host masses span  $\sim 0.12\text{--}0.75 M_{\odot}$ , corresponding to sub-solar main-sequence stars from early M to mid K types. The hosts are most likely located in the bulge and the inferred projected separations place the planets beyond the snowlines of their hosts, illustrating the power of microlensing to probe wide-separation planets at large distances. Figure 6 presents the Bayesian posterior distributions of  $M_p$ , showing that the inferred planet masses for all events are consistent with that of Saturn.

## 9. SUMMARY AND DISCUSSION

We have analyzed three microlensing events, KMT-2021-BLG-0852, KMT-2024-BLG-2005, and KMT-2025-BLG-0481, that share the common feature of short-lived positive anomalies on the wings of otherwise standard microlensing light curves. The timing and sign of these deviations indicate that they arise from peripheral caustics produced by planetary-mass companions. Motivated by this interpretation, we modeled each event within a binary-lens framework and tested plausible alternative explanations, including binary-source models,

**Table 4.** Physical lens parameters.

Parameter	KMT-2021-BLG-0852	KMT-2024-BLG-2005	KMT-2025-BLG-0481
$M_h (M_\odot)$	$0.75^{+0.26}_{-0.27}$	$0.12^{+0.17}_{-0.06}$	$0.22^{+0.31}_{-0.13}$
$M_p (M_J)$	$0.49^{+0.17}_{-0.17}$	$0.16^{+0.24}_{-0.09}$	$0.59^{+0.85}_{-0.34}$
$D_L$ (kpc)	$7.23^{+0.83}_{-1.03}$	$7.72^{+1.00}_{-1.06}$	$7.98^{+1.13}_{-1.44}$
$a_\perp$ (au)	$7.78^{+0.89}_{-1.11}$	$1.12^{+0.15}_{-0.15}$	$2.18^{+0.31}_{-0.39}$
$p_{\text{disk}}$	5%	19%	32%
$p_{\text{bulge}}$	95%	81%	68%

higher mass-ratio binary lenses, and degenerate caustic geometries. In all cases, the planetary solution is preferred, and the anomaly morphology provides strong leverage for resolving the relevant degeneracies.

Using Bayesian estimates of the physical lens parameters constrained by the event timescale and angular Einstein radius, we infer sub-solar-mass host stars with companions consistent with Saturn-mass planets. The inferred projected separations place the planets in the cold-giant regime beyond the snowline, underscoring the continued role of microlensing in mapping the population of wide-orbit planets around low-mass hosts.

Continued improvements in time-domain coverage and multi-survey baselines are rapidly increasing the number of microlensing planet detections, enabling increasingly detailed investigations of planet formation and evolution. The three Saturn-mass planets reported here are especially valuable because they probe the transition regime between ice giants and gas giants, where formation outcomes are highly sensitive to the onset and termination of runaway gas accretion. Consequently, these systems provide strong empirical tests of competing planet-formation pathways and will sharpen demographic constraints on cold giant planets orbiting low-mass stars.

The lensing event KMT-2021-BLG-0852 illustrates a pathway for distinguishing a free-floating planet from a wide-separation bound planet. Because the primary event has very low magnification ( $A_{\text{max}} \sim 1.15$ ), it could easily go unnoticed unless attention is drawn by the planetary anomaly, and in some cases it may remain un-

detectable even after such follow-up scrutiny. Nevertheless, an FFP interpretation can still be rejected when the planetary perturbation exhibits a complex morphology induced by shear from a host star, as in this event and in MOA-bin-1 (Bennett et al. 2012). Such events are therefore valuable for probing the observational transition between clearly identifiable 2L1S planetary systems and candidates for truly free-floating planets.

#### ACKNOWLEDGEMENTS

C.H. was supported by the National Research Foundation of Korea (NRF) grant funded by the Korea government (MSIT: RS-2025-21073000). Work by C.U.Lee research was supported by the Korea Astronomy and Space Science Institute under the R&D program (Project No. 2025-1-830-05) supervised by the Ministry of Science and ICT. This research has made use of the KMTNet system operated by the Korea Astronomy and Space Science Institute (KASI) at three host sites of CTIO in Chile, SAAO in South Africa, and SSO in Australia. Data transfer from the host site to KASI was supported by the Korea Research Environment Open NETwork (KREONET). The OGLE project has received funding from the Polish National Science Centre grant OPUS-28 2024/55/B/ST9/00447 to AU. H.Y. and W.Z. acknowledge support by the National Natural Science Foundation of China (Grant No. 12133005). The MOA project is supported by JSPS KAKENHI Grant Number JP16H06287, JP22H00153 and 23KK0060. C.R. was supported by the Research fellowship of the Alexander von Humboldt Foundation.

#### REFERENCES

Alard, C., & Lupton, R. H. 1998, ApJ, 503, 325, doi: [10.1086/305984](https://doi.org/10.1086/305984)

Alibert, Y., Mordasini, C., Benz, W., & Winisdoerffer, C. 2005, A&A, 434, A343, doi: [10.1051/0004-6361:20042032](https://doi.org/10.1051/0004-6361:20042032)

Bennett, D. P., Sumi, T., Bond, I. A., et al. 2012, ApJ, 757, 119, doi: [10.1088/0004-637X/757/2/119](https://doi.org/10.1088/0004-637X/757/2/119)

Bensby, T., Yee, J. C., Feltzing, S., et al. 2013, A&A, 549, A247, doi: [10.1051/0004-6361/201220678](https://doi.org/10.1051/0004-6361/201220678)

Bond, I. A., Abe, F., Dodd, R. J., et al. 2001, MNRAS, 327, 868, doi: [doi:10.1046/j.1365-8711.2001.04776.x](https://doi.org/10.1046/j.1365-8711.2001.04776.x)

Collaboration, G., Vallenari, A., Brown, A. G. A., et al. 2023, A&A, 674, A1, doi: [10.1051/0004-6361/202243940](https://doi.org/10.1051/0004-6361/202243940)

Fortney, J. J., Marley, M. S., & Barnes, J. W. 2007, ApJ, 659, 1661, doi: [10.1086/512120](https://doi.org/10.1086/512120)

Gaudi, B. S. 1998, ApJ, 506, 533, doi: [10.1086/306256](https://doi.org/10.1086/306256)

—. 2012, ARA&A, 50, 411, doi: [10.1146/annurev-astro-081811-125518](https://doi.org/10.1146/annurev-astro-081811-125518)

Gaudi, B. S., & Gould, A. 1997, ApJ, 486, 85, doi: [10.1086/304491](https://doi.org/10.1086/304491)

Gould, A., & Loeb, A. 1992, ApJ, 396, 104, doi: [10.1086/171700](https://doi.org/10.1086/171700)

Griest, K., & Hu, W. 1992, ApJ, 397, 362, doi: [10.1086/17179](https://doi.org/10.1086/17179)

Griest, K., & Safizadeh, N. 1998, ApJ, 500, 37, doi: [10.1086/30572](https://doi.org/10.1086/30572)

Han, C., Albrow, M. D., Lee, C.-U., et al. 2024a, A&A, 689, A209, doi: [10.1051/0004-6361/202450873](https://doi.org/10.1051/0004-6361/202450873)

Han, C., Bond, I. A., Lee, C.-U., et al. 2024b, A&A, 687, A225, doi: [10.1051/0004-6361/202450221](https://doi.org/10.1051/0004-6361/202450221)

Holtzman, J. A., Watson, A. M., Baum, W. A., et al. 1998, AJ, 115, 1946, doi: [10.1086/300336](https://doi.org/10.1086/300336)

Hwang, K.-H., Udalski, A., Shvartzvald, Y., et al. 2018, AJ, 155, 20, doi: [10.3847/1538-3881/aa992f](https://doi.org/10.3847/1538-3881/aa992f)

Hwang, K.-H., Choi, J.-Y., Bond, I. A., et al. 2013, ApJ, 778, 55, doi: [10.1088/0004-637X/778/1/55](https://doi.org/10.1088/0004-637X/778/1/55)

Ida, S., & Lin, D. N. C. 2004, ApJ, 604, 388, doi: [10.1086/381724](https://doi.org/10.1086/381724)

Jung, Y. K., Han, C., Udalski, A., et al. 2021, AJ, 161, 293, doi: [10.3847/1538-3881/abf8bd](https://doi.org/10.3847/1538-3881/abf8bd)

Jung, Y. K., Zang, W., Han, C., et al. 2022, AJ, 164, 262, doi: [10.3847/1538-3881/ac9c5c](https://doi.org/10.3847/1538-3881/ac9c5c)

Kennedy, G. M., & Kenyon, S. J. 2008, ApJ, 673, 502, doi: [10.1086/524130](https://doi.org/10.1086/524130)

Kervella, P., Thévenin, F., Di Folco, E., & Ségransan, D. 2004, A&A, 426, 29, doi: [10.1051/0004-6361:20035930](https://doi.org/10.1051/0004-6361:20035930)

Kim, S.-L., Lee, C.-U. and Park, B.-G., Kim, D.-J., et al. 2016, JKAS, 49, 37, doi: [10.5303/JKAS.2016.49.1.37](https://doi.org/10.5303/JKAS.2016.49.1.37)

Mao, S., & Paczyński, B. 1991, ApJL, 374, L37, doi: [10.1086/186066](https://doi.org/10.1086/186066)

Nataf, D. M., Gould, A., Fouqué, P., et al. 2013, ApJ, 769, 88, doi: [10.1088/0004-637X/769/2/88](https://doi.org/10.1088/0004-637X/769/2/88)

Pollack, J. B., Hubickyj, O., Bodenheimer, P., et al. 1996, Icarus, 124, 62, doi: [10.1006/icar.1996.0190](https://doi.org/10.1006/icar.1996.0190)

Shin, I.-G., Yee, J. C., Gould, A., et al. 2019, AJ, 158, 199, doi: [10.3847/1538-3881/ab46a5](https://doi.org/10.3847/1538-3881/ab46a5)

Stevenson, D. J. 1982, Planetary and Space Science, 30, 755, doi: [10.1016/0032-0633\(82\)90108-8](https://doi.org/10.1016/0032-0633(82)90108-8)

Sumi, T., Buckley, D. A. H., Kutyrev, A. S., et al. 2025, AJ, 170, 338, doi: [10.3847/1538-3881/ae14f5](https://doi.org/10.3847/1538-3881/ae14f5)

Sumi, T., Abe, F., Bond, I. A., et al. 2003, ApJ, 591, 204, doi: [doi:10.1086/375212](https://doi.org/10.1086/375212)

Tomaney, A. B., & Crots, A. P. S. 1996, AJ, 112, 2872, doi: [10.1086/118228](https://doi.org/10.1086/118228)

Udalski, A., Szymański, M. K., & Szymański, G. 2015, Acta Astronomica, 65, 1, doi: [10.48550/arXiv.1504.0596](https://doi.org/10.48550/arXiv.1504.0596)

Winn, J. N., & Fabrycky, D. C. 2015, ARA&A, 53, 409, doi: [10.1146/annurev-astro-082214-122246](https://doi.org/10.1146/annurev-astro-082214-122246)

Woźniak, P. 2000, Acta Astronomica, 50, 421, doi: [10.48550/arXiv.astro-ph/0012143](https://doi.org/10.48550/arXiv.astro-ph/0012143)

Yee, J. C., Shvartzvald, Y., Gal-Yam, A., et al. 2012, ApJ, 755, 102, doi: [10.1088/0004-637X/755/2/102](https://doi.org/10.1088/0004-637X/755/2/102)

Yoo, J., DePoy, D. L., A., G.-Y., et al. 2004, ApJ, 603, 13, doi: [10.1086/381241](https://doi.org/10.1086/381241)